

## The Impact of Hydrogen Bonding on Amide $^1\text{H}$ Chemical Shift Anisotropy Studied by Cross-Correlated Relaxation and Liquid Crystal NMR Spectroscopy

Lishan Yao,<sup>†,‡</sup> Alexander Grishaev,<sup>‡</sup> Gabriel Cornilescu,<sup>§</sup> and Ad Bax<sup>\*,‡</sup>

Qingdao Institute of Bioenergy and Bioprocess Technology, Chinese Academy of Sciences, Qingdao 266061, China, Laboratory of Chemical Physics, NIDDK, National Institutes of Health, Building 5, Room 126 NIH, Bethesda, Maryland 20892-0520, and National Magnetic Resonance Facility, Madison, Wisconsin 53706

Received April 28, 2010; E-mail: bax@nih.gov

**Abstract:** Site-specific  $^1\text{H}$  chemical shift anisotropy (CSA) tensors have been derived for the well-ordered backbone amide moieties in the B3 domain of protein G (GB3). Experimental input data include residual chemical shift anisotropy (RCSA), measured in six mutants that align differently relative to the static magnetic field when dissolved in a liquid crystalline Pf1 suspension, and cross-correlated relaxation rates between the  $^1\text{H}^{\text{N}}$  CSA tensor and either the  $^1\text{H}-^{15}\text{N}$ , the  $^1\text{H}-^{13}\text{C}'$ , or the  $^1\text{H}-^{13}\text{C}^{\alpha}$  dipolar interactions. Analyses with the assumption that the  $^1\text{H}^{\text{N}}$  CSA tensor is symmetric with respect to the peptide plane (three-parameter fit) or without this premise (five-parameter fit) yield very similar results, confirming the robustness of the experimental input data, and that, to a good approximation, one of the principal components orients orthogonal to the peptide plane.  $^1\text{H}^{\text{N}}$  CSA tensors are found to deviate strongly from axial symmetry, with the most shielded tensor component roughly parallel to the N-H vector, and the least shielded component orthogonal to the peptide plane. DFT calculations on pairs of *N*-methyl acetamide and acetamide in H-bonded geometries taken from the GB3 X-ray structure correlate with experimental data and indicate that H-bonding effects dominate variations in the  $^1\text{H}^{\text{N}}$  CSA. Using experimentally derived  $^1\text{H}^{\text{N}}$  CSA tensors, the optimal relaxation interference effect needed for narrowest  $^1\text{H}^{\text{N}}$  TROSY line widths is found at  $\sim 1200$  MHz.

### Introduction

Isotropic chemical shifts are key parameters in NMR spectroscopy, enabling signals from different nuclei of any given type in a molecule to be distinguished. Chemical shift values often can be determined at very high precision, up to 6 orders of magnitude higher than the range of chemical shift values observed. Although chemical shifts clearly are exquisitely sensitive to molecular structure, our understanding of the relation between structure and chemical shift remains relatively rudimentary in all but the simplest model systems.<sup>1</sup> However, the potential richness of information contained in chemical shifts has stimulated efforts to develop a better quantitative understanding of the relationship between these parameters and molecular structure, particularly in proteins.<sup>2–10</sup> Magnetic

shielding of a nucleus by its surrounding electrons is a process that lends itself well to quantum chemical calculations. For peptides and proteins, such quantum calculations now make it possible to rapidly predict chemical shift values of  $^{15}\text{N}$ ,  $^{13}\text{C}$ , and  $^1\text{H}$  nuclei on the basis of the molecule's experimentally determined structure.<sup>11,12</sup> Perhaps surprisingly, predictions of isotropic chemical shifts based on simple empirical database analysis yield values that agree somewhat better with experimentally observed shifts.<sup>13–15</sup> These latter types of analysis, however, do not provide much insight in the individual factors contributing to chemical shielding. For that purpose, it is necessary to take a step back and evaluate the impact of structural factors on chemical shielding anisotropy (CSA). For example, for backbone  $^{13}\text{C}'$  nuclei in small proteins, accurate CSA values have been obtained by both solution and solid state NMR.<sup>16,17</sup> These results clearly confirmed prior results<sup>18–20</sup>

<sup>†</sup> Qingdao Institute of Bioenergy and Bioprocess Technology, Chinese Academy of Sciences.

<sup>‡</sup> Laboratory of Chemical Physics, NIDDK, National Institutes of Health.

<sup>§</sup> National Magnetic Resonance Facility.

- (1) Jameson, C. J. *Annu. Rev. Phys. Chem.* **1996**, *47*, 135–169.
- (2) McConnell, H. M. *J. Chem. Phys.* **1957**, *27*, 226–229.
- (3) de Dios, A. C.; Pearson, J. G.; Oldfield, E. *Science* **1993**, *260*, 1491–1496.
- (4) Osapay, K.; Case, D. A. *J. Am. Chem. Soc.* **1991**, *113*, 9436–9444.
- (5) Williamson, M. P.; Asakura, T. *J. Magn. Reson. B* **1993**, *101*, 63–71.
- (6) Ando, I.; Kameda, T.; Asakawa, N.; Kuroki, S.; Kurosu, H. *J. Mol. Struct.* **1998**, *441*, 213–230.
- (7) Saito, H. *Magn. Reson. Chem.* **1986**, *24*, 835–852.
- (8) Barfield, M. *J. Am. Chem. Soc.* **2002**, *124*, 4158–4168.
- (9) Case, D. A. *Curr. Opin. Struct. Biol.* **1998**, *8*, 624–630.
- (10) Moon, S.; Case, D. A. *J. Biomol. NMR* **2007**, *38*, 139–150.

- (11) Xu, X. P.; Case, D. A. *J. Biomol. NMR* **2001**, *21*, 321–333.
- (12) Vila, J. A.; Arnautova, Y. A.; Martin, O. A.; Scheraga, H. A. *Proc. Natl. Acad. Sci. U.S.A.* **2009**, *106*, 16972–16977.
- (13) Shen, Y.; Bax, A. *J. Biomol. NMR* **2007**, *38*, 289–302.
- (14) Neal, S.; Nip, A. M.; Zhang, H. Y.; Wishart, D. S. *J. Biomol. NMR* **2003**, *26*, 215–240.
- (15) Kohlhoff, K. J.; Robustelli, P.; Cavalli, A.; Salvatella, X.; Vendruscolo, M. *J. Am. Chem. Soc.* **2009**, *131*, 13894–13895.
- (16) Loth, K.; Pelupessy, P.; Bodenhausen, G. *J. Am. Chem. Soc.* **2005**, *127*, 6062–6068.
- (17) Wylie, B. J.; Sperling, L. J.; Frericks, H. L.; Shah, G. J.; Franks, W. T.; Rienstra, C. M. *J. Am. Chem. Soc.* **2007**, *129*, 5318–5319.
- (18) Teng, Q.; Iqbal, M.; Cross, T. A. *J. Am. Chem. Soc.* **1992**, *114*, 5312–5321.

which indicate that variation in isotropic  $^{13}\text{C}'$  chemical shifts can be attributed almost entirely to differences in the  $\sigma_{YY}$  component of the shielding tensor.<sup>21–23</sup> The latter is a steep function of both backbone torsion angles and hydrogen bond strength.<sup>22–24</sup> For backbone amide  $^{15}\text{N}$ , the range of isotropic shifts observed in proteins is large, spanning more than 20 ppm for residues of any given type, but both computational and empirical efforts to correlate chemical shift changes to structural parameters have been challenging. Much effort has been devoted to measuring the  $^{15}\text{N}$  CSA tensor in proteins,<sup>16,25–28</sup> both by solution and solid-state NMR methods, but only recently has a consensus started to emerge.<sup>17,29</sup> As indicated by DFT calculations, amide  $^{15}\text{N}$  CSA is impacted by many variables, including backbone and side chain torsion angles, hydrogen bonding, and residue type.<sup>30–32</sup> We have recently shown<sup>29</sup> that  $^{15}\text{N}$  CSA magnitudes of the third IgG binding domain of protein G (GB3, dissolved in a medium containing liquid crystalline Pf1) correlate well with those obtained from spinning sideband analysis of slow magic angle spinning (MAS) solid-state NMR measurements<sup>17</sup> on a closely homologous domain. Asymmetry of the CSA tensor was found to be dominated by the backbone torsion angles.

The solution NMR experiments used for characterizing the  $^{15}\text{N}$  CSA tensor also contain information on the backbone carbonyl and amide proton CSA. These measurements were carried out on six conservative GB3 mutants that adopt different average orientations relative to the director of a liquid crystalline Pf1 suspension.<sup>33</sup> Small differences between isotropic  $^{15}\text{N}$  chemical shifts and those measured under the six different orientations in the liquid crystalline matrix result from incomplete averaging of the  $^{15}\text{N}$  CSA tensor, giving rise to residual chemical shift anisotropy (RCSA). These RCSA values are measured from three-dimensional (3D) HNC0 triple resonance spectra, which contain  $^{13}\text{C}'$  and  $^1\text{H}^{\text{N}}$  RCSA in the other two dimensions of the spectrum. Simultaneously, by recording the HNC0 spectrum in the  $^1\text{H}$ -coupled mode,  $^{15}\text{N}$ – $^1\text{H}$  residual dipolar couplings (RDCs) are obtained that define the alignment tensor (Saupe matrix) of the mutant proteins relative to the magnetic field. For  $^{13}\text{C}'$ , we find that the RCSA values agree to within experimental error with  $^{13}\text{C}'$  CSA values extracted from slow MAS solid state NMR experiments.<sup>17</sup> For this reason,

analysis of this RCSA data is not further pursued as it would not improve on the solid state NMR results ( $^{13}\text{C}'$  RCSA values in GB3 are included as Supporting Information). Instead, we focus here on the  $^1\text{H}^{\text{N}}$  CSA.  $^1\text{H}$  CSA values, expressed in ppm, are much smaller than for  $^{13}\text{C}$  and  $^{15}\text{N}$ , but experimental knowledge of these tensors is important to gain further insights on the parameters that govern variations in  $^1\text{H}^{\text{N}}$  isotropic chemical shifts. Moreover,  $^1\text{H}^{\text{N}}$  CSA is key to resolution enhancement of amide groups in multidimensional TROSY experiments<sup>34,35</sup> which, besides utilizing relaxation interference between  $^{15}\text{N}$ – $^1\text{H}^{\text{N}}$  dipolar and  $^{15}\text{N}$  CSA interactions for enhancing  $^{15}\text{N}$  resolution, rely on relaxation interference between the  $^1\text{H}$ – $^{15}\text{N}$  dipolar and  $^1\text{H}^{\text{N}}$  CSA for increasing resolution in the  $^1\text{H}$  dimension.

It has long been known that increasing hydrogen bond strength causes a downfield  $^1\text{H}$  chemical shift, accompanied by an increase in  $^1\text{H}$  CSA.<sup>36</sup> However, relative to  $^{13}\text{C}'$  and  $^{15}\text{N}$ , the CSA of amide protons in peptide bonds has been studied rather sparsely.<sup>37–39</sup> Cross-correlated relaxation rates between  $^1\text{H}$ – $^{15}\text{N}$  dipolar and  $^1\text{H}^{\text{N}}$  CSA mechanisms have been interpreted in terms of a “reduced CSA”, which does not separate the magnitude of the CSA tensor and its asymmetry from its orientation relative to the amide group.<sup>40</sup> Nevertheless, these early measurements indicated much larger site-to-site variation in the  $^1\text{H}^{\text{N}}$  CSA than for backbone  $^{15}\text{N}$  and  $^{13}\text{C}'$ .  $^1\text{H}^{\text{N}}$  CSA values measured for ubiquitin, assuming that these tensors are uniform within  $\alpha$ -helices and within  $\beta$ -sheet, indicated that the CSA tensors are nearly fully rhombic, with the magnitude of the CSA about 35% larger in  $\beta$ -sheet compared to  $\alpha$ -helix.<sup>41</sup> A more recent study by Loth et al. determined site-specific  $^1\text{H}^{\text{N}}$  CSA values in ubiquitin from measurement of three different relaxation interference mechanisms.<sup>16</sup> Their study confirms that shielding is highest in the direction parallel to the N–H bond, and lowest in the direction orthogonal to the peptide plane. Variations in isotropic chemical shifts were attributed almost entirely to variations in this latter component. With the isotropic amide  $^1\text{H}$  chemical shifts correlating closely with trans-hydrogen-bond  $^3J_{\text{NC}'}$  couplings,<sup>8,42</sup> and the latter closely correlating with hydrogen bond strength and geometry,<sup>8,43</sup> this provides an indirect link between  $^1\text{H}^{\text{N}}$  CSA and hydrogen bonding.

With only three cross-correlated relaxation rates available to determine the three independent parameters of the  $^1\text{H}^{\text{N}}$  CSA tensor, when assumed to be symmetric relative to the peptide plane, Loth et al. report the precision of their  $^1\text{H}^{\text{N}}$  CSA values to be considerably lower than for  $^{13}\text{C}'$  and  $^{15}\text{N}$ .<sup>16</sup> The present study aims to get highly accurate site-specific  $^1\text{H}^{\text{N}}$  CSA values by using a larger number of experimental observables (six RCSA values and four cross-correlated relaxation rates). Moreover, we carry out our RCSA measurements on perdeuterated GB3, with the backbone amides back-exchanged to become protonated.

- (19) Lumsden, M. D.; Wasylishen, R. E.; Eichele, K.; Schindler, M.; Penner, G. H.; Power, W. P.; Curtis, R. D. *J. Am. Chem. Soc.* **1994**, *116*, 1403–1413.
- (20) Wei, Y. F.; Lee, D. K.; Ramamoorthy, A. *J. Am. Chem. Soc.* **2001**, *123*, 6118–6126.
- (21) Oas, T. G.; Hartzell, C. J.; McMahon, T. J.; Drobny, G. P.; Dahlquist, F. W. *J. Am. Chem. Soc.* **1987**, *109*, 5956–5962.
- (22) Asakawa, N.; Kuroki, S.; Kurosu, H.; Ando, I.; Shoji, A.; Ozaki, T. *J. Am. Chem. Soc.* **1992**, *114*, 3261–3265.
- (23) Markwick, P. R. L.; Sattler, M. *J. Am. Chem. Soc.* **2004**, *126*, 11424–11425.
- (24) Burton, R. A.; Tjandra, N. *J. Am. Chem. Soc.* **2007**, *129*, 1321–1326.
- (25) Fushman, D.; Tjandra, N.; Cowburn, D. *J. Am. Chem. Soc.* **1998**, *120*, 10947–10952.
- (26) Damberg, P.; Jarvet, J.; Graslund, A. *J. Am. Chem. Soc.* **2005**, *127*, 1995–2005.
- (27) Kroenke, C. D.; Rance, M.; Palmer, A. G. *J. Am. Chem. Soc.* **1999**, *121*, 10119–10125.
- (28) Wylie, B. J.; Franks, W. T.; Rienstra, C. M. *J. Phys. Chem. B* **2006**, *110*, 10926–10936.
- (29) Yao, L.; Grishaev, A.; Cornilescu, G.; Bax, A. *J. Am. Chem. Soc.* **2010**, *132*, 4295–4309.
- (30) Walling, A. E.; Pargas, R. E.; deDios, A. C. *J. Phys. Chem. A* **1997**, *101*, 7299–7303.
- (31) Bader, R. *J. Phys. Chem. B* **2009**, *113*, 347–358.
- (32) Benda, L.; Bour, P.; Muller, N.; Sychrovsky, V. *J. Phys. Chem. B* **2009**, *113*, 5273–5281.
- (33) Yao, L. S.; Bax, A. *J. Am. Chem. Soc.* **2007**, *129*, 11326–11327.

- (34) Pervushin, K.; Riek, R.; Wider, G.; Wuthrich, K. *Proc. Natl. Acad. Sci. U.S.A.* **1997**, *94*, 12366–12371.
- (35) Salzmann, M.; Wider, G.; Pervushin, K.; Senn, H.; Wuthrich, K. *J. Am. Chem. Soc.* **1999**, *121*, 844–848.
- (36) Berglund, B.; Vaughan, R. W. *J. Chem. Phys.* **1980**, *73*, 2037–2043.
- (37) Reimer, J. A.; Vaughan, R. W. *J. Magn. Reson.* **1980**, *41*, 483–491.
- (38) Wu, C. H.; Ramamoorthy, A.; Gierasch, L. M.; Opella, S. J. *J. Am. Chem. Soc.* **1995**, *117*, 6148–6149.
- (39) Gerald, R.; Bernhard, T.; Haeberlen, U.; Rendell, J.; Opella, S. *J. Am. Chem. Soc.* **1993**, *115*, 777–782.
- (40) Tjandra, N.; Bax, A. *J. Am. Chem. Soc.* **1997**, *119*, 8076–8082.
- (41) Cornilescu, G.; Bax, A. *J. Am. Chem. Soc.* **2000**, *122*, 10143–10154.
- (42) Cordier, F.; Grzesiek, S. *J. Am. Chem. Soc.* **1999**, *121*, 1601–1602.
- (43) Cornilescu, G.; Ramirez, B. E.; Frank, M. K.; Clore, G. M.; Gronenborn, A. M.; Bax, A. *J. Am. Chem. Soc.* **1999**, *121*, 6275–6279.

The use of deuteration removes the impact from remote protons that can otherwise interfere with the precise measurement of RCSAs. Our experimental data are of a quality that is sufficient to permit fitting of the individual  $^1\text{H}^{\text{N}}$  CSA tensors in GB3 without the assumption of symmetry with respect to the peptide plane, i.e., using five adjustable parameters. Correlations between our experimentally determined  $^1\text{H}^{\text{N}}$  CSA values and the local structure in GB3, together with DFT calculations on *N*-methyl acetamide (NMA) H-bonded to acetamide, are then used to gain a more quantitative understanding of the relation between hydrogen-bond geometry and  $^1\text{H}^{\text{N}}$  CSA.

## Materials and Methods

**NMR Spectroscopy.** The experimental data used for determining  $^1\text{H}^{\text{N}}$  CSA values consisted of RCSA measurements on six GB3 mutants that align differently relative to the magnetic field in a liquid crystalline Pf1 suspension, complemented by four cross-correlated relaxation experiments. The  $^1\text{H}^{\text{N}}$  RCSA values were extracted from the same 3D spectra previously used for  $^{15}\text{N}$  RCSA measurement, and experimental details regarding the collection and analysis of this data have been described previously.<sup>29</sup> In brief, the  $^1\text{H}^{\text{N}}$  chemical shifts were measured in the  $^1\text{H}$  dimension of a 3D HNCO experiment, carried out for each mutant in a liquid crystalline Pf1 suspension, once under static conditions and once under slow magic angle spinning ( $\sim 600$  Hz). The latter destroys any average order of the liquid crystal relative to the magnetic field and thereby removes any net RDC and RCSA contributions caused by interaction between the Pf1 and GB3, without complications caused by small chemical shift changes that could potentially result from changes in the sample and buffer composition. The impact of small differences in temperature on the  $^1\text{H}$  chemical shifts between the static and MAS HNCO spectra was accounted for, *a posteriori*, by evaluating the correlation between observed chemical shift changes and the measured temperature coefficients of  $^1\text{H}^{\text{N}}$ ,  $^{15}\text{N}$ , and  $^{13}\text{C}'$ .<sup>29</sup>

A sample containing 4 mM of the GB3 mutant T11K K19A V42E, uniformly enriched in  $^{15}\text{N}$ ,  $^{13}\text{C}$ , and  $^2\text{H}$ , and dissolved in 25 mM sodium phosphate buffer, pH 6.5, 50 mM NaCl, 0.05% w/v  $\text{NaN}_3$ , was used to measure the cross-correlated relaxation rates between  $^1\text{H}^{\text{N}}$  CSA and  $^1\text{H}-^{15}\text{N}$  as well as  $^1\text{H}-^{13}\text{C}'$  and  $^1\text{H}-^{13}\text{C}^\alpha$  dipolar interactions. NMR experiments were carried out on Bruker spectrometers operating at 500 and 600 MHz and equipped with *z*-axis gradient, triple resonance, cryogenic probeheads.

$^1\text{H}^{\text{N}}$  transverse cross-correlated relaxation rates were measured for perdeuterated GB3 mutant T11K K19A V42E (but with a small amount of residual protonation resulting from the use of protonated glucose in the 99%  $\text{D}_2\text{O}$  growth medium) for the following interactions:  $^1\text{H}^{\text{N}}$  CSA/ $^1\text{H}^{\text{N}}$ -N dipole-dipole ( $\Gamma^{\text{CSA,HN}}$ );  $^1\text{H}^{\text{N}}_i$  CSA/ $^1\text{H}^{\text{N}}_{i-1}$  (where the subscript refers to the residue number on which the atom resides) dipole-dipole ( $\Gamma^{\text{CSA,HC}^\alpha}$ );  $^1\text{H}^{\text{N}}_i$  CSA/ $^1\text{H}^{\text{N}}_{i-1}$ - $\text{C}^\alpha_i$  dipole-dipole (intraresidue  $\Gamma^{\text{CSA,HC}^\alpha_i}$ );  $^1\text{H}^{\text{N}}_i$  CSA/ $^1\text{H}^{\text{N}}_{i-1}$ - $\text{C}^\alpha_{i-1}$  dipole-dipole (sequential  $\Gamma^{\text{CSA,HC}^\alpha_{i-1}}$ ). Experiments used to measure these rates are all based on the  $^1\text{H}$ -detected  $^1\text{H}-^{15}\text{N}$  HSQC pulse sequence,<sup>44</sup> and mostly employ pulse schemes similar to those described by Loth et al.<sup>16</sup> For measurement of  $\Gamma^{\text{CSA,HN}}$ , a transverse relaxation delay of duration  $T$  was inserted between  $90^\circ$  ( $^1\text{H}, ^{15}\text{N}$ ) pulses that transfer magnetization back from  $^{15}\text{N}$  to  $^1\text{H}$  and the start of the  $^1\text{H}$  acquisition, in the absence of  $^{15}\text{N}$  decoupling during  $T$  and the subsequent  $^1\text{H}$  acquisition period (Supporting Information (SI), Figure S1). The two  $^1\text{H}^{\text{N}}-\{^{15}\text{N}\}$  doublet components, separated by  $^1J_{\text{HN}}$ , relax at rates governed by the sum and the difference of the  $^1\text{H}^{\text{N}}$  CSA and  $^{15}\text{N}-^1\text{H}^{\text{N}}$  dipolar interaction. Durations of  $T$  were: 10, 30, 50, 70, 90, 110, 130, and 150 ms. Acquisition times were 150 ( $^{15}\text{N}$ ) and 160 ms ( $^1\text{H}$ ), with data matrices consisting of  $200^* \times 1536^*$  points, where  $N^*$  refers to  $N$  complex data points.

(44) Bodenhausen, G.; Ruben, D. J. *Chem. Phys. Lett.* **1980**, *69*, 185–189.

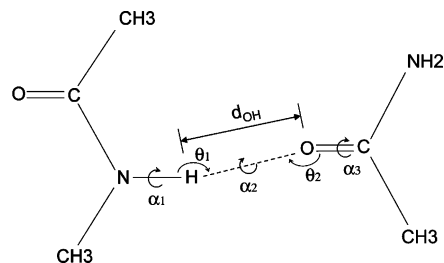


**Figure 1.** Diagram of *N*-methyl acetamide hydrogen bonded to acetamide, depicting the geometric parameters used in this study.  $d_{\text{OH}}$  denotes the distance between H and O atoms,  $(\theta_1, \theta_2)$  denote the angles  $\angle\text{N}-\text{H}-\text{O}$  and  $\angle\text{H}-\text{O}-\text{C}$ ,  $(\alpha_1, \alpha_2, \alpha_3)$  are the dihedral angles  $\text{C}-\text{N}-\text{H}-\text{O}$ ,  $\text{N}-\text{H}-\text{O}-\text{C}$ ,  $\text{H}-\text{O}-\text{C}-\text{CH}_3$ .

Measurement of  $\Gamma^{\text{CSA,HC}^\alpha}$  is carried out using the pulse scheme of Figure S2 (SI), which relies on the E.COSY effect to separate the  $^1\text{H}^{\text{N}}-[^{13}\text{C}'_{i-1}]$  doublet components. If  $\text{H}_x\text{C}'_z\text{N}_z$  terms were to develop during the spin-echo relaxation delay (i.e., if no  $^{15}\text{N}$  decoupling were used), longitudinal cross-correlated relaxation between the  $^{15}\text{N}$  CSA and the  $^{15}\text{N}-^{13}\text{C}'$  dipolar interaction would contribute to the decay rate of the detected  $^1\text{H}^{\text{N}}$  magnetization. To remove the effects from this longitudinal  $^{15}\text{N}$  CSA/ $^{15}\text{N}-^{13}\text{C}'_{i-1}$  relaxation interference, composite pulse  $^{15}\text{N}$  decoupling was applied during the relaxation delay,  $T$ . Durations of  $T$  were 2, 30, 50, 70, 90, 110, 130, and 150 ms; acquisition times and data matrices were the same as for the  $\Gamma^{\text{CSA,NH}}$  measurements, above.

Measurement of intraresidue  $\Gamma^{\text{CSA,HC}^\alpha_i}$  and sequential  $\Gamma^{\text{CSA,HC}^\alpha_{i-1}}$  rates was carried out with the pulse sequence of Figure S3 (SI), briefly discussed in the Results and Discussion section. Durations of the relaxation delays  $T$  were: 2, 30, 50, 70, 90, 110, 130, and 150 ms. Acquisition times were 300 ( $^{15}\text{N}$ ) and 125 ( $^1\text{H}$ ) ms, with data matrices consisting of  $400^* \times 1200^*$  points.

All spectra were processed and analyzed using the software package NMRPipe.<sup>45</sup> Peak positions and intensities were determined by parabolic interpolation. Apparent relaxation rates were determined from two-parameter exponential fits of peak intensities. The cross-correlated relaxation rates  $\Gamma^{\text{CSA,HN}}$  ( $\Gamma^{\text{CSA,HC}^\alpha}$ ) were calculated from the apparent relaxation rate difference when the  $^{15}\text{N}$  ( $^{13}\text{C}'$ ), involved in the dipolar coupling term, is in the  $|\alpha\rangle$  or  $|\beta\rangle$  spin state. The  $\Gamma^{\text{CSA,HC}^\alpha_i}$  and  $\Gamma^{\text{CSA,HC}^\alpha_{i-1}}$  were calculated using the following equations

$$\Gamma^{\text{CSA,HC}^\alpha_{i-1}} = (R_2^{\alpha\alpha} - R_2^{\beta\alpha} + R_2^{\alpha\beta} - R_2^{\beta\beta})/4 \quad (1a)$$

$$\Gamma^{\text{CSA,HC}^\alpha_i} = (R_2^{\alpha\alpha} - R_2^{\beta\alpha} + R_2^{\beta\alpha} - R_2^{\beta\beta})/4 \quad (1b)$$

where the first and the second superscript denotes the respective spin state of the preceding and intraresidue  $^{13}\text{C}^\alpha$  nucleus, and  $R_2$  is the relaxation rate determined from the exponential fit.

**Quantum Chemical Calculations.** Two alanine dipeptide fragments ( $\text{HCO}(\text{NHCHCH}_3\text{CO})_2\text{H}$ ) were built with backbone torsion angles corresponding to those of E24-T25 and L5-V6 in the NMR-refined X-ray structure (PDB entry 2OED),<sup>46</sup> where the first pair is taken from GB3's  $\alpha$ -helix, and the second pair has typical  $\beta$ -sheet backbone torsion angles. Calculations on these fragments were used to evaluate the impact of backbone torsion angles on  $^1\text{H}^{\text{N}}$  CSA in the absence of hydrogen bonding.

*N*-Methyl acetamide (NMA) H-bonded to acetamide was used to systematically study the effect of hydrogen bonding on the amide  $^1\text{H}^{\text{N}}$  CSA. Six geometrical parameters ( $d_{\text{OH}}$ ,  $\alpha_1$ ,  $\alpha_2$ ,  $\alpha_3$ ,  $\theta_1$ ,  $\theta_2$ ) define the position of acetamide relative to NMA (Figure 1). To explore the impact of  $d_{\text{OH}}$  on  $^1\text{H}^{\text{N}}$  CSA, the distance was stepped from 1.8

(45) Delaglio, F.; Grzesiek, S.; Vuister, G. W.; Zhu, G.; Pfeifer, J.; Bax, A. *J. Biomol. NMR* **1995**, *6*, 277–293.

(46) Ulmer, T. S.; Ramirez, B. E.; Delaglio, F.; Bax, A. *J. Am. Chem. Soc.* **2003**, *125*, 9179–9191.

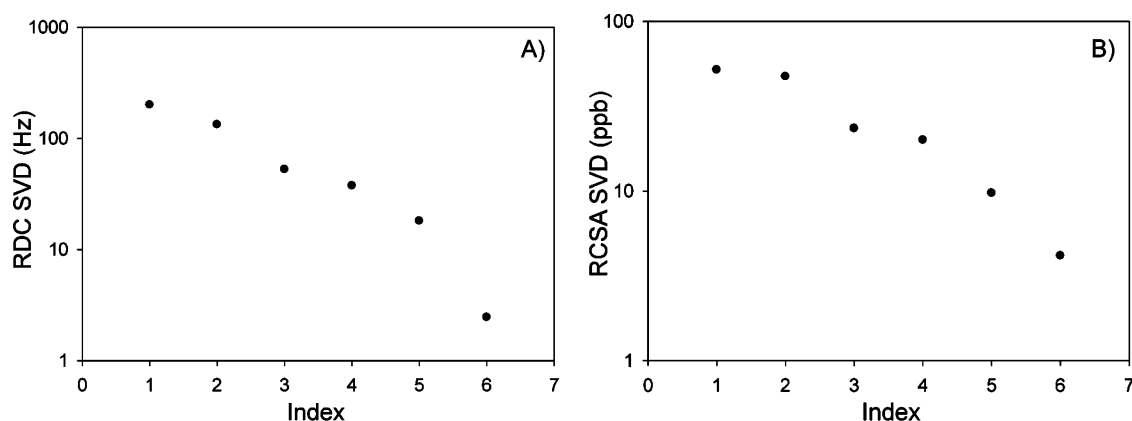


**Figure 2.** Independence of RDC (panel A) and RCSA (panel B) data sets assessed by singular value decomposition (SVD). SVD analysis was performed for 51 (48) residues for which all six RDCs (RCSAs) were available.

to 2.6 Å (1.8, 1.9, 2.0, 2.1, 2.2, 2.4 and 2.6), with the other 5 degrees of freedom constrained by  $(\theta_1, \theta_2)$  at  $180^\circ$  and  $(\alpha_1, \alpha_2, \alpha_3)$  at  $0^\circ$ .

The  $^1\text{H}$  CSA of 34 NMA-acetamide model systems was also calculated, with H-bond geometrical parameters corresponding to those of the 34 backbone-backbone H-bonds in the experimental GB3 structure. All models were geometry optimized at the B3LYP/6-311+G\*\* level<sup>47</sup> while constraining  $(d_{\text{OH}}, \alpha_1, \alpha_2, \alpha_3, \theta_1, \theta_2)$  to the experimental values of the 2OED PDB entry<sup>46</sup> and the distance between the H-bond-donating N and H-bond-accepting O atom fixed. Chemical shielding tensors were calculated using the GIAO method<sup>48,49</sup> at the B3LYP/aug-cc-pvtz level.<sup>50</sup> The chemical shift tensor, which includes the isotropic contribution,  $\delta_{\text{isotropic}}$ , was computed as  $\delta_{ii} = \delta_{\text{isotropic}} - \sigma_{ii}$  ( $i = X, Y, Z$ ), where  $\delta_{\text{isotropic}}$  is 32.775 ppm,<sup>51</sup> the absolute chemical shift of TMS at 298 K, and  $\sigma_{ii}$  are the calculated CSA tensor principal components.

## Results and Discussion

**RDC and RCSA.** In order to derive the residue-specific  $^1\text{H}^{\text{N}}$  CSA tensors from RCSA data recorded for the previously studied six GB3 mutants, which align differently relative to the magnetic field, the corresponding protein alignment tensors were determined by best fitting RDCs to the known experimental structure.<sup>52</sup> For this purpose, one-bond  $^1\text{H}-^{15}\text{N}$  RDCs,  $^1D_{\text{NH}}$ , were extracted from HNC0 experiments, recorded in the absence of  $^1\text{H}$  decoupling during  $^{15}\text{N}$  evolution. For 52 out of a total of 56 residues,  $^1D_{\text{NH}}$  couplings could be measured at high accuracy for all six mutants. With the exception of the highly mobile residue G41, SECONDA analysis<sup>53</sup> of the RDCs showed the data to be highly self-consistent (Figure S4 (SI)). This result indicates that the backbone structure and dynamics of the six mutants, as reflected in their  $^1D_{\text{NH}}$  couplings, do not differ substantially between the different mutants. Singular value decomposition (SVD) was used to evaluate the degree of independence of the six sets of RDCs, excluding G41. Consistent with our earlier findings,<sup>33,54</sup> the six GB3 mutants aligned in

Pf1 span the entire five-dimensional (5D) alignment space (Figure 2A) with a ratio between the fifth and sixth singular value of 7.4, where the last mode is primarily noise from measurement error.

With molecular orientations covering the entire 5D alignment space, in principle the five components of each  $^1\text{H}^{\text{N}}$  CSA tensor can be derived directly from the RCSA values measured for the six mutants. However, the relative accuracy of  $^1\text{H}^{\text{N}}$  RCSA is considerably lower than for  $^1D_{\text{NH}}$  couplings, and a SVD analysis of the six sets of RCSAs (Figure 2B) shows a ratio between the fifth and sixth component of only 2.3, suggesting that for the fifth alignment (after decomposing alignments in the orthogonal 5D alignment space), RCSA values are not much above the measurement noise represented by the sixth SVD value. Addition of random, Gaussian distributed noise to GB3 amides RCSA values predicted for each of the six alignments, using  $^1\text{H}^{\text{N}}$  CSA tensor parameters taken from our earlier study,<sup>41</sup> yields a similar ratio between the fifth and sixth SVD value when the noise amplitude is adjusted to 1.0 ppb. This 1.0 ppb value therefore corresponds to the estimated error for our experimental  $^1\text{H}^{\text{N}}$  RCSA values. With typical experimental RCSA values falling in the  $\pm 10$  ppb range (Table S1 (SI)), the relative large RCSA measurement error propagates to substantial random error in the extracted  $^1\text{H}^{\text{N}}$  CSA tensors, which is indistinguishable from the intrinsic residue-by-residue variability we aim to study. To improve the  $^1\text{H}^{\text{N}}$  CSA accuracy, additional CSA-dependent parameters therefore need to be measured and included in the CSA fitting procedure.

**Transverse  $^1\text{H}$  CSA Dipolar Cross-Correlated Relaxation Rates.** Transverse cross-correlated relaxation rates between the  $^1\text{H}^{\text{N}}$  CSA and four different dipolar couplings involving  $^1\text{H}^{\text{N}}$  were measured, including  $^1\text{H}-^{15}\text{N}$  ( $\Gamma^{\text{CSA,HN}}$ ), intraresidue  $^1\text{H}^{\text{N}}-^{13}\text{C}^\alpha$  ( $\Gamma^{\text{CSA,HC}\alpha}$ ), as well as dipolar couplings to  $^{13}\text{C}'$  ( $\Gamma^{\text{CSA,HC}'}$ ) and  $^{13}\text{C}^\alpha$  ( $\Gamma^{\text{CSA,HC}\alpha-1}$ ) on the preceding residue. These cross-correlated relaxation rates were derived from the difference in relaxation rates of the transverse  $^1\text{H}$  spin operator when the X nucleus is in the  $|\alpha\rangle$  and  $|\beta\rangle$  spin states. For the  $\Gamma^{\text{CSA,HN}}$  measurement,  $^1\text{H}^{\text{N}}$  signals corresponding to  $^{15}\text{N}$  in  $|\alpha\rangle$  and  $|\beta\rangle$  spin states are well separated (by  $^1J_{\text{NH}} \approx -93$  Hz; Figure 3A). In contrast, for  $\Gamma^{\text{CSA,HC}'}$  measurement the  $^2J_{\text{HC}'}$  splitting is insufficiently large to resolve the  $^1\text{H}^{\text{N}}-\{^{13}\text{C}'\}$  doublet components. However, these components are easily separated in an E.COSY-type manner<sup>55,56</sup> in the  $^{15}\text{N}$  dimension, taking advantage of the relatively large  $^1J_{\text{NC}'}$  ( $\sim -15$  Hz) coupling (Figure 3B, Figure S2 (SI)). However, the same type of experiment is

(47) Frisch, M. J.; et al. *Gaussian 03*, Revision C.02; Gaussian Inc.: Wallingford, CT, 2004.

(48) Ditchfield, R. *Mol. Phys.* **1974**, *27*, 789–807.

(49) Wolinski, K.; Hinton, J. F.; Pulay, P. *J. Am. Chem. Soc.* **1990**, *112*, 8251–8260.

(50) Becke, A. D. *J. Chem. Phys.* **1993**, *98*, 5648–5652.

(51) Jackowski, K.; Wilczek, M.; Pecul, M.; Sadlej, J. *J. Phys. Chem. A* **2000**, *104*, 9806–9806.

(52) Losonczi, J. A.; Andrec, M.; Fischer, M. W. F.; Prestegard, J. H. *J. Magn. Reson.* **1999**, *138*, 334–342.

(53) Hus, J. C.; Peti, W.; Griesinger, C.; Bruschweiler, R. *J. Am. Chem. Soc.* **2003**, *125*, 5596–5597.

(54) Yao, L.; Vogeli, B.; Torchia, D. A.; Bax, A. *J. Phys. Chem. B* **2008**, *112*, 6045–6056.

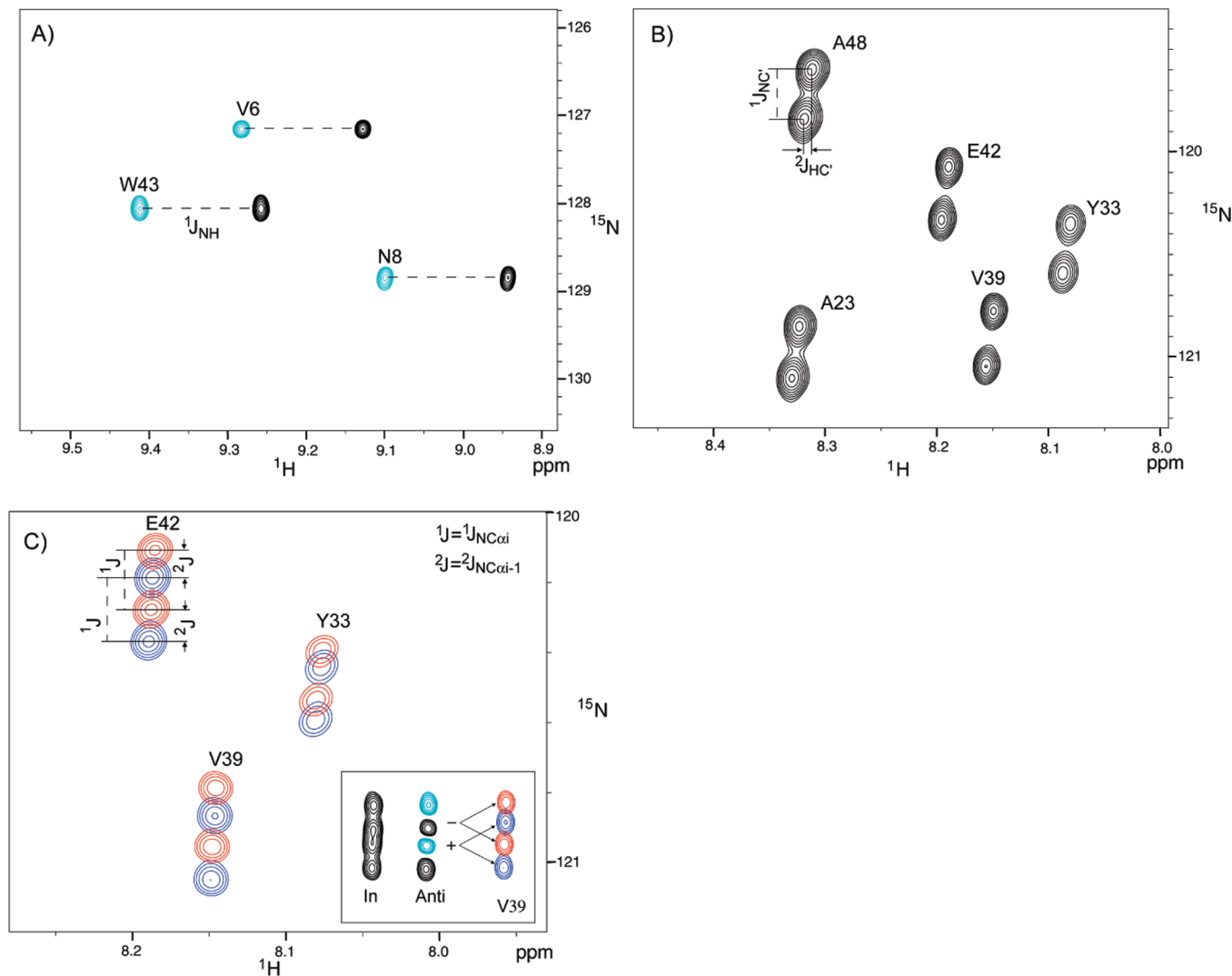


**Figure 3.** Small regions extracted from transverse  $^1\text{H}^{\text{N}}$  CSA/ $^1\text{H}^{\text{N}}$ -X dipolar cross-correlated relaxation rate measurements, recorded at 600 MHz  $^1\text{H}$  frequency. (A)  $\Gamma^{\text{CSA},\text{HN}}$  ( $^1\text{H}^{\text{N}}$  CSA/ $^1\text{H}^{\text{N}}$ - $^{15}\text{N}$  dipole), (B)  $\Gamma^{\text{CSA},\text{HC}'}$  ( $^1\text{H}^{\text{N}}$  CSA/ $^1\text{H}^{\text{N}}$ - $^{13}\text{C}'$  dipole), (C)  $\Gamma^{\text{CSA},\text{HC}\alpha}$  ( $^1\text{H}^{\text{N}}$  CSA/ $^1\text{H}^{\text{N}}$ -intra  $^{13}\text{C}\alpha$  dipole),  $\Gamma^{\text{CSA},\text{HC}\alpha-1}$  ( $^1\text{H}^{\text{N}}$  CSA/ $^1\text{H}^{\text{N}}$ -preceding  $^{13}\text{C}\alpha$  dipole). In (A), cyan and black contours represent the positive and negative intensities, corresponding to  $^{15}\text{N}$  in  $|\alpha\rangle$  and  $|\beta\rangle$  spin states. In (B), the E.COSY mechanism separates  $^1\text{H}^{\text{N}}$  signals with  $^{13}\text{C}'$  in  $|\alpha\rangle$  and  $|\beta\rangle$  spin states. In (C), two interleaved experiments corresponding to spectra that are in-phase and anti-phase with respect to the preceding  $^{13}\text{C}\alpha_{i-1}$  were used to separate the doublet of doublets caused by intra  $^2J_{\text{HC}\alpha}$  ( $^1J_{\text{NC}\alpha}$ ) and sequential  $^3J_{\text{HC}\alpha}$  ( $^2J_{\text{NC}\alpha}$ ) couplings. The spectra corresponding to blue and red contours are obtained by adding and subtracting the anti-phase spectrum to/from the in-phase spectrum, respectively, as illustrated in the inset for V39. Relaxation rates were measured with the pulse schemes of Figures S1, S2, and S3 (SI).

insufficient for  $\Gamma^{\text{CSA},\text{HC}\alpha}$  and  $\Gamma^{\text{CSA},\text{HC}\alpha-1}$  measurement because the smaller  $^1J_{\text{NC}\alpha}$  and  $^2J_{\text{NC}\alpha}$  couplings result in generally unresolvable doublet-of-doublet signals for each  $^{13}\text{C}\alpha$ -coupled  $^1\text{H}$ - $^{15}\text{N}$  correlation (Figure 3C). Instead, we developed an interleaved in-phase and anti-phase (with respect to  $\text{C}\alpha_{i-1}$ ) 2D-HN(CO) type experiment, recorded with and without  $^{13}\text{C}\alpha$  decoupling during a  $(2J_{\text{C}\alpha\text{C}'})^{-1}$  fraction of the pulse sequence (Figure S3 (SI)). This procedure generates doublets of doublets that are in-phase with respect to both  $^{13}\text{C}\alpha_{i-1}$  and  $^{13}\text{C}\alpha_i$ , or anti-phase with respect to  $^{13}\text{C}\alpha_{i-1}$  but in-phase with respect to  $^{13}\text{C}\alpha_i$  (Figure 3C). By taking the sum or the difference of the in-phase and anti-phase spectra, clean separation into two separate doublets is obtained (Figure 3C), permitting measurement of the  $\Gamma^{\text{CSA},\text{HC}\alpha}$  and  $\Gamma^{\text{CSA},\text{HC}\alpha-1}$  relaxation rates.

The cross-correlated relaxation rates are plotted in Figure 4. After excluding the residues found to have the lowest-order parameters in the earlier relaxation study by Hall and Fushman,<sup>57</sup> including Q2, K10-E15, A20, D40-G41, and A48, and two residues (T25; E27) due to partial resonance overlap, the average  $\Gamma^{\text{CSA},\text{HN}}$  is  $1.58 \pm 0.40 \text{ s}^{-1}$ . The average  $\Gamma^{\text{CSA},\text{HC}'}$  is smaller in magnitude,  $-0.30 \pm 0.09 \text{ s}^{-1}$ , the latter being comparable to  $\langle \Gamma^{\text{CSA},\text{HC}\alpha} \rangle = -0.39 \pm 0.10 \text{ s}^{-1}$ ; near-zero values are measured for  $\Gamma^{\text{CSA},\text{HC}\alpha-1}$  ( $\langle \Gamma^{\text{CSA},\text{HC}\alpha-1} \rangle = 0.02 \pm 0.04 \text{ s}^{-1}$ ). In part, the differences in average magnitude are caused by the difference in dipolar coupling for the four types of cross-correlation effects, but even after taking this into account the averages of the four types of cross-correlation rates remain quite different in average magnitude (Figure 4), reflecting the orientation of the corresponding dipolar vector in the frame of the  $^1\text{H}^{\text{N}}$  CSA tensor. For all four types of cross-correlation rates, the variation seen in  $\Gamma$  values is

(55) Griesinger, C.; Sørensen, O. W.; Ernst, R. R. *J. Magn. Reson.* **1987**, *75*, 474–492.

(56) Delaglio, F.; Torchia, D. A.; Bax, A. *J. Biomol. NMR* **1991**, *1*, 439–446.

(57) Hall, J. B.; Fushman, D. *J. Biomol. NMR* **2003**, *27*, 261–275.

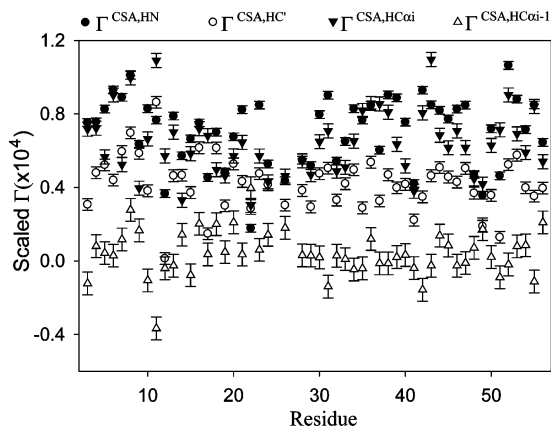


**Figure 4.** The normalized transverse  $^1\text{H}^{\text{N}}$  CSA dipolar cross-correlated relaxation rates  $\Gamma^{\text{CSA,HN}}$ ,  $\Gamma^{\text{CSA,HC'}}$ ,  $\Gamma^{\text{CSA,HCai}}$  and  $\Gamma^{\text{CSA,HCai-1}}$  at 600 MHz  $^1\text{H}$  frequency. The experimental rates  $\Gamma^{\text{CSA,HN}}$  were normalized by dividing by the dipolar interaction constant  $-\mu_0\gamma_{\text{H}}\gamma_{\text{X}}h/8\pi^3r_{\text{HX}}^3$  (21.657 kHz for  $\Gamma^{\text{CSA,HN}}$ ;  $-7.038$  kHz for  $\Gamma^{\text{CSA,HC'}}$ ;  $-5.896$  kHz for  $\Gamma^{\text{CSA,HCai}}$ ;  $-3.644$  kHz for  $\Gamma^{\text{CSA,HCai-1}}$ ), where  $\mu_0$  is the magnetic permittivity of vacuum,  $h$  is Planck's constant,  $\gamma_{\text{X}}$  is the magnetogyric ratio of spin X, and  $r_{\text{HX}}$  is the distance between nuclei H and X. These dipolar interaction constants are based on a librational and vibrationally adjusted N–H bond length of  $r_{\text{NH}} = 1.04$  Å,<sup>58</sup> and average bond lengths and angles taken from Engh and Huber.<sup>59</sup>

far higher than the experimental measurement error and is dominated by the site-to-site variability of the  $^1\text{H}^{\text{N}}$  CSA tensor, but also contains a small contribution from the anisotropic rotational diffusion of GB3 and potential variations in internal backbone dynamics, which impact the applicable spectral density terms.

**Extracting Residue-Specific  $^1\text{H}^{\text{N}}$  CSA Tensors.** Fitting of the residue-specific  $^1\text{H}^{\text{N}}$  CSA tensors to the cross-correlated relaxation rates requires knowledge of the GB3 rotational diffusion tensor. In our previous  $^{15}\text{N}$  CSA study, the diffusion tensor of the mutant K4A K19E V42E was determined from  $^{15}\text{N}$   $R_1$  and  $R_2$  rates. The sample used in the current study is the perdeuterated mutant T11K K19A V42E. To account for any potential diffusion tensor change caused by differences in charge distribution on the protein surface and protein concentration, we measured the  $^{15}\text{N}$  CSA/N–H dipole cross-correlated transverse relaxation rates and compared these rates with those previously reported<sup>29</sup> for mutant K4A K19E V42E. With a Pearson's correlation coefficient  $R_p = 0.99$  and a slope 1.04, a very close correlation was obtained (Figure S5 (SI)), indicating a 4% slower diffusion rate for the sample used in the present study, but indistinguishable anisotropy and orientation of the diffusion tensor. In subsequent fitting of  $^1\text{H}^{\text{N}}$  CSA tensors, the principal components of the axially symmetric diffusion tensor previously determined for K4A K19E V42E, were therefore scaled down by 1.04, yielding  $D_{\text{XX}} = D_{\text{YY}} = 4.49 \times 10^7$  s $^{-1}$ ;  $D_{\text{ZZ}} = 6.12 \times 10^7$  s $^{-1}$ , or an apparent rotational correlation time  $\tau_c = 3.3$  ns. Excluding the previously identified residues with elevated internal dynamics (Q2, K10-E15, A20, D40-G41, and A48)<sup>57</sup> and overlapping residues (T25 and E27), a uniform generalized order parameter,  $S^2 = 0.903$  (derived in our previous  $^{15}\text{N}$  CSA study),<sup>29</sup> was used for the analysis of the cross-correlated relaxation rates. In principle, high-frequency spectral density terms resulting from internal backbone dynamics also contribute to the relaxation rates. However, as reported by Hall and Fushman,<sup>57</sup> the longest internal correlation time,  $\tau_e$ , in the well-structured region of the protein used for our analysis is 56 ps, corresponding to  $\leq 1\%$

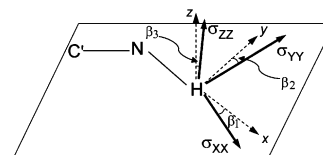


**Figure 5.** The coordinate system and angles used to describe the orientation of the CSA tensor. The  $z$  axis is orthogonal to the plane defined by C'–N–H, while the  $x$  and  $y$  axes are in this plane, with  $x$  parallel to the N–H bond. The  $\beta_1$ ,  $\beta_2$ , and  $\beta_3$  values are defined by the angles between  $x$ ,  $y$ , and  $z$  axes and the  $\sigma_{\text{XX}}$ ,  $\sigma_{\text{YY}}$ , and  $\sigma_{\text{ZZ}}$  axes, respectively.

contribution to the cross-correlation rates, which is smaller than the measurement error and therefore ignored in the fitting.

In our analysis, we simultaneously fit the  $^1\text{H}$  RCSAs under six different alignment orientations, together with the  $\Gamma^{\text{CSA,HN}}$ ,  $\Gamma^{\text{CSA,HC'}}$ ,  $\Gamma^{\text{CSA,HCai}}$  and  $\Gamma^{\text{CSA,HCai-1}}$  relaxation rates. Three Euler angles ( $\omega_1$ ,  $\omega_2$ ,  $\omega_3$ ,  $z$ - $y$ - $z$  convention) are used to describe the orientation of each  $^1\text{H}^{\text{N}}$  CSA tensor relative to the peptide plane, defined by C', N, and H $^{\text{N}}$  atoms. With the restriction that  $\sigma_{\text{XX}} + \sigma_{\text{YY}} + \sigma_{\text{ZZ}} = 0$ , two parameters suffice to define its principal components, and a total of five parameters therefore fully define the tensor.

The site-specific  $^1\text{H}$  CSA values, resulting from fitting the 10 values experimentally observed for each  $^1\text{H}^{\text{N}}$ , are plotted in Figure 6 (and also listed in Table S4 (SI)). Average values are:  $\sigma_{\text{ZZ}} = -6.2 \pm 1.0$ ,  $\sigma_{\text{YY}} = 0.5 \pm 0.9$ ,  $\sigma_{\text{XX}} = 5.7 \pm 1.3$  ppm. Averaged over all fitted residues, the average tensor magnitude,  $\Delta\sigma = \sigma_{\text{ZZ}} - (\sigma_{\text{XX}} + \sigma_{\text{YY}})/2$ , equals  $-9.4 \pm 1.6$  ppm. For the  $\beta$ -strand residues, the average CSA magnitude is given by  $\langle\Delta\sigma\rangle = -10.3 \pm 1.3$  ppm; for  $\alpha$ -helix we find  $\langle\Delta\sigma\rangle = -8.2 \pm 1.5$  ppm. The smaller absolute  $\Delta\sigma$  in  $\alpha$ -helix contrasts with the  $^{15}\text{N}$  CSA, which has a larger magnitude in  $\alpha$ -helix than in  $\beta$ -strand.<sup>17,29,60</sup> The CSA tensors all are quite asymmetric, with average  $\eta$  parameters ( $\eta = (\sigma_{\text{YY}} - \sigma_{\text{XX}})/\sigma_{\text{ZZ}}$ ) of  $0.90 \pm 0.22$  in  $\beta$ -strand, and  $0.76 \pm 0.25$  in  $\alpha$ -helix.

The chemical shielding anisotropy tensor is defined as the traceless part of the full shielding tensor. Evaluation of the impact of geometric and H-bonding parameters on the shielding in any given direction requires evaluation of the full shielding tensor, including its trace. To facilitate comparison with experimental chemical shifts, we utilize the oppositely signed chemical shift tensor, which is defined to include its isotropic component:  $\delta_{ii} = \delta_{\text{isotropic}} - \sigma_{ii}$ . Average values of  $\delta_{\text{ZZ}} = 15.5 \pm 1.3$ ,  $\delta_{\text{YY}} = 8.3 \pm 1.1$ ,  $\delta_{\text{XX}} = 2.2 \pm 0.7$  ppm are obtained for  $\beta$ -sheet, and  $13.6 \pm 1.6$ ,  $7.5 \pm 1.1$ ,  $3.3 \pm 0.7$  ppm for  $\alpha$ -helix. Remarkably, these data indicate that, even while on average  $\beta$ -sheet isotropic shifts are about 0.5 ppm downfield relative to the  $\alpha$ -helical values, the  $\delta_{\text{XX}}$  component in  $\beta$ -sheet, roughly parallel to the N–H vector (Figure 5), falls upfield from  $\delta_{\text{XX}}$  in  $\alpha$ -helix. This effect is more than offset by deshielding in the Y (by 0.8 ppm) and Z (by 1.9 ppm) directions.

The Euler angles defining the orientation of each  $^1\text{H}^{\text{N}}$  CSA tensor are listed in Table S4 (SI). The average  $\omega_2$  angle is  $-3.8 \pm 9.0^\circ$ , indicating that the  $^1\text{H}^{\text{N}}$  CSA tensor is nearly symmetric with respect to the peptide plane. The relatively small value of  $\omega_2$  results in  $\omega_1$  and  $\omega_3$  rotations that are nearly about the same axis, such that the opposite signed values of  $\omega_1$  and  $\omega_3$  around the  $z$  axis largely cancel one another, making the spread in mostly oppositely signed  $\omega_1$  and  $\omega_3$  values not very meaningful. To overcome this problem in evaluating the variation in tensor orientation, three quantities  $\beta_1$ ,  $\beta_2$ ,  $\beta_3$  are defined as the angles

(58) Yao, L.; Voegeli, B.; Ying, J. F.; Bax, A. *J. Am. Chem. Soc.* **2008**, *130*, 16518–16520.

(59) Engh, R. A.; Huber, R. *Acta Crystallogr., Sect A* **1991**, *47*, 392–400.

(60) Cai, L.; Fushman, D.; Kosov, D. S. *J. Biomol. NMR* **2008**, *41*, 77–88.

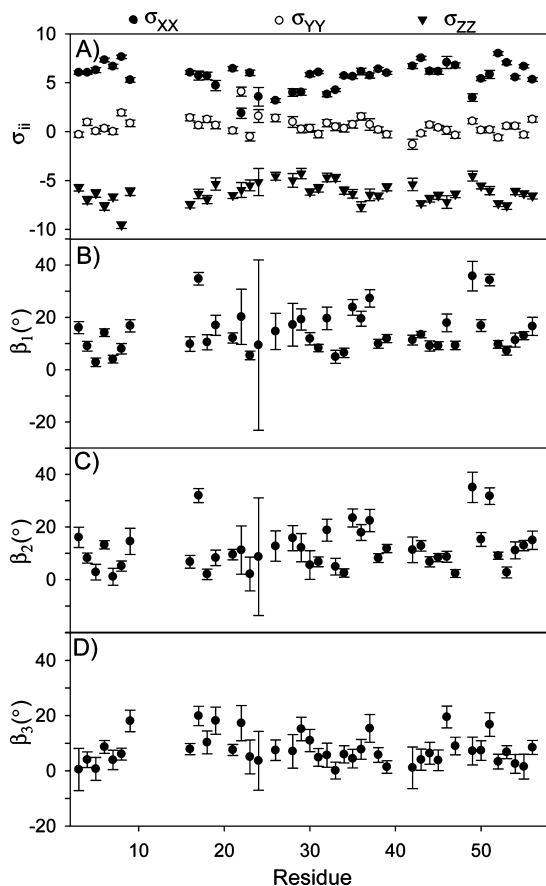


**Figure 6.** Residue-specific  $^1\text{H}^{\text{N}}$  CSA parameters,  $\sigma_{xx}$ ,  $\sigma_{yy}$ ,  $\sigma_{zz}$ , derived from RCSA and cross-correlated relaxation data, using a five-parameter CSA tensor fit (no symmetry is imposed relative to the peptide plane). (A) Values of the principal components of the CSA tensors. (B) Angle  $\beta_1$  between  $\sigma_{xx}$  and  $x$ ; (C)  $\beta_2$  between  $\sigma_{yy}$  and  $y$ ; (D)  $\beta_3$  between  $\sigma_{zz}$  and  $z$  (Figure 5). Small  $\beta_3$  values show that for most residues  $\sigma_{xx}$  and  $\sigma_{yy}$  are located nearly in the peptide plane. Error bars correspond to the results of 100 Monte Carlo calculations, where Gaussian noise with an amplitude corresponding to the estimated root-mean-square measurement error was added to the experimental input data.

between  $\sigma_{xx}$  and  $x$ ,  $\sigma_{yy}$  and  $y$ ,  $\sigma_{zz}$  and  $z$ , respectively (Figure 5). The average over all 42  $\beta_1$  values is  $14 \pm 8^\circ$ . Because  $\sigma_{zz}$  is nearly orthogonal to the peptide plane,  $\beta_2$  is strongly correlated with  $\beta_1$  (Figure S6 (SI)). The angle  $\beta_3$  is smaller than  $10^\circ$  for 32 residues, with an average value over all 42 residues of  $\langle \beta_3 \rangle = 8 \pm 6^\circ$ . A limitation of the  $\beta_i$  parameters is that they do not distinguish the direction in which  $\sigma_{ii}$  is rotated away from the  $i$  axis, which potentially is problematic for  $\beta_1$ . This issue can be resolved by introducing a parameter  $\beta_1'$ , defined as the angle between the  $x$  axis and the projection of  $\sigma_{xx}$  on the  $xy$  plane. If  $\beta_1'$  is defined as positive when the projection of  $\sigma_{xx}$  on the  $y$  axis is negative, the average  $\beta_1'$  is  $10 \pm 10^\circ$ , with 37 out of 42 residues having positive values (Table S4 (SI)).

Previously, a correlation between  $^1\text{H}^{\text{N}}$  CSA and isotropic chemical shifts was noted for backbone amides in ubiquitin.<sup>16,61</sup> Somewhat stronger correlations are found in our present study of GB3 (Figure 7A) where, for example, the correlation coefficient  $R_P$  between  $\delta_{zz}$  and  $\delta_{\text{isotropic}}$  equals 0.89, versus 0.82 for ubiquitin (excluding the flexible residues L71-G76). In contrast to  $\delta_{zz}$  and  $\delta_{yy}$ ,  $\delta_{xx}$  shows only a very weak correlation with  $\delta_{\text{isotropic}}$ .

**Origin of  $^1\text{H}^{\text{N}}$  CSA Variations.** The relatively large residue-by-residue variations in  $\Delta\sigma$ , and in the angles defining the

orientation of the  $^1\text{H}^{\text{N}}$  CSA tensors, raise the important question regarding the physical causes underlying these variations. For comparison, the 5% fluctuation in CSA amplitude and  $2.5^\circ$  in orientation of the  $^{15}\text{N}$  CSA tensor are much smaller, when evaluated over the same set of GB3 residues.<sup>29</sup> No statistically significant correlation is observed between  $\sigma_{ii}$  of the  $^1\text{H}^{\text{N}}$  CSA tensor and any of the  $\sigma_{ij}$  components of the corresponding  $^{15}\text{N}$  CSA, nor between  $\delta_{ii}$  of  $^1\text{H}^{\text{N}}$  and any  $^{15}\text{N}$   $\delta_{ij}$  value (data not shown). These results suggest that  $^1\text{H}^{\text{N}}$  CSA has a quite different dependence on local structure than the  $^{15}\text{N}$  CSA and also that the relative impact of local structure is much larger for  $^1\text{H}^{\text{N}}$  than for  $^{15}\text{N}$ .

The smaller average  $\Delta\sigma$  observed in  $\alpha$ -helix compared that in to  $\beta$ -sheet might suggest that the backbone dihedral angles impact the  $^1\text{H}$  CSA. However, when calculating the  $^1\text{H}^{\text{N}}$  CSA of an alanine dipeptide using DFT, ( $\delta_{zz}$ ,  $\delta_{yy}$ ,  $\delta_{xx}$ ) values of 12.9, 6.6, 1.0 ppm are obtained for the helical conformation, versus 11.7, 5.5, 3.0 ppm for a  $\beta$ -strand geometry. The larger CSA calculated for  $\alpha$ -helical backbone torsion angles is opposite to the experimental results, suggesting that unlike what was found for  $^{15}\text{N}$ ,  $^1\text{H}^{\text{N}}$  CSA differences between the  $\alpha$ -helix and  $\beta$ -sheet are not dominated by their difference in backbone torsion angles.

It has long been known that the isotropic  $^1\text{H}$  chemical shift depends strongly on hydrogen bonding,<sup>62–64</sup> but the impact of hydrogen bonding on  $^1\text{H}$  chemical shift anisotropy has been explored to a much lesser extent. In proteins, Cordier and Grzesiek demonstrated that the isotropic  $^1\text{H}^{\text{N}}$  chemical shift correlates closely with the magnitude of  $^3\text{J}_{\text{NC}}$  couplings across the H-bond,<sup>42</sup> which in turn related directly to hydrogen-bond strength.<sup>43</sup> The strong correlations we observe between  $\delta_{\text{isotropic}}$  and both  $\delta_{zz}$  and  $\delta_{yy}$  (Figure 7A) imply that hydrogen bonding also dominates the variations seen for the  $\delta_{zz}$  and  $\delta_{yy}$  components. To further evaluate this relation, we carried out DFT calculations for the model compound NMA, H-bonded to acetamide (Figure 1). Values of  $\delta_{zz}$ ,  $\delta_{yy}$ ,  $\delta_{xx}$  were derived as a function of hydrogen-bond length,  $d_{\text{OH}}$ , while restraining ( $\theta_1$ ,  $\theta_2$ ) at  $180^\circ$  and ( $\alpha_1$ ,  $\alpha_2$ ,  $\alpha_3$ ) at  $0^\circ$  (Figure 8). These calculations show that  $\delta_{zz}$  and  $\delta_{yy}$ , but not  $\delta_{xx}$ , decrease with increasing  $d_{\text{OH}}$ . By fitting  $\delta_{zz}$ ,  $\delta_{yy}$ , and  $\delta_{xx}$  to equations of the form  $\delta_{ii} = a + b \exp(-c \cdot d_{\text{OH}})$ ,  $c$  values of 3.0, 2.8, and  $1.1 \text{ \AA}^{-1}$  were obtained, respectively, confirming the stronger dependence of  $\delta_{zz}$  and  $\delta_{yy}$  on  $d_{\text{OH}}$ . The effect of hydrogen bonding on CSA agrees with analyses by Sitkoff and Case,<sup>65</sup> who used DFT to study NMA H-bonded to water. They attributed the changes in the principal components of the CSA tensor to the  $d_{\text{OH}}$ -dependence of the polarization of the electron density in the N–H direction, which perturbs the induced magnetic field perpendicular to the N–H vector more than in the parallel direction. As a result  $\delta_{zz}$  and  $\delta_{yy}$ , the components approximately perpendicular to the N–H axis, are more influenced by the H-bond strength than  $\delta_{xx}$ . This reasoning assumes that the  $^1\text{H}^{\text{N}}$  shielding is dominated by the diamagnetic component of the CSA, applicable to amide protons with electrons primarily in the  $1s$  orbital, where the paramagnetic term is very small.

As expected, changing  $\theta_2$  away from  $180^\circ$  while keeping  $d_{\text{OH}}$  fixed (at  $1.8 \text{ \AA}$ ), such as to improve the H-bond interaction to one of the two carbonyl lone pairs, has an effect similar to shortening  $d_{\text{OH}}$ , resulting in downfield changes of  $\delta_{zz}$  and  $\delta_{yy}$ .

(62) Ditchfield, R. *J. Chem. Phys.* **1976**, *65*, 3123–3133.

(63) Crothers, D. M.; Hilbers, C. W.; Shulman, R. G. *Proc. Natl. Acad. Sci. U.S.A.* **1973**, *70*, 2899–2901.

(64) Wagner, G.; Pardi, A.; Wuthrich, K. *J. Am. Chem. Soc.* **1983**, *105*, 5948–5949.

(65) Sitkoff, D.; Case, D. A. *J. Am. Chem. Soc.* **1997**, *119*, 12262–12273.

(61) Tjandra, N.; Bax, A. *J. Am. Chem. Soc.* **1997**, *119*, 8076–8082.

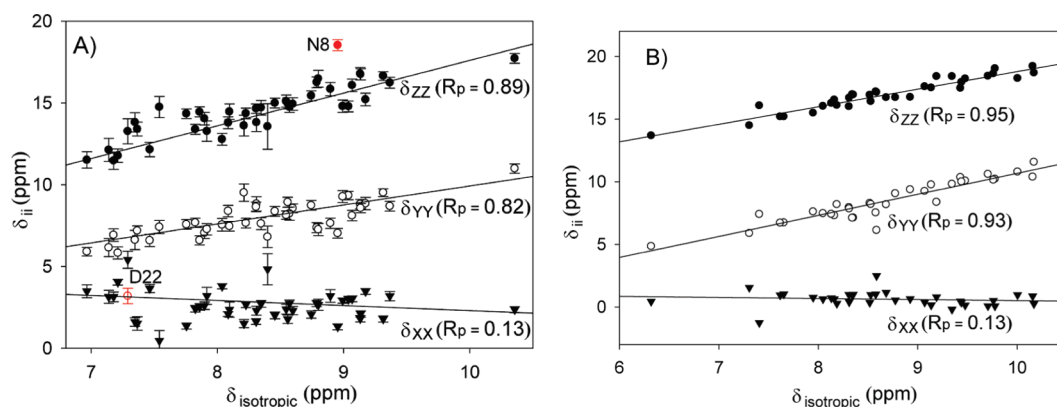


**Figure 7.** Correlations between the principal components of the chemical shift tensor  $\delta_{ii}$  ( $i = X, Y, Z$ ) and the isotropic chemical shift,  $\delta_{isotropic}$ . (A) Experimental  $\delta_{isotropic}$  values and  $^1\text{H}^{\text{N}}$  CSA tensor components obtained from fitting to the experimental RCSA and cross-correlated relaxation rates, and (B)  $\delta_{isotropic}$  values and CSA tensor components obtained from DFT calculations. For (A), all 42 experimentally obtained CSA tensor values are shown, and the three best fitted lines correspond to  $\delta_{ZZ} = 1.79\delta_{isotropic} - 0.38$  ppm;  $\delta_{YY} = 1.22\delta_{isotropic} - 2.28$  ppm;  $\delta_{XX} = -0.17\delta_{isotropic} + 4.03$  ppm. Two outliers ( $\delta_{ZZ}$  of N8 and  $\delta_{YY}$  of D22) are not included in the fit, nor in the calculation of the Pearson's correlation coefficients,  $R_p$ . For (B), data are restricted to the 34 backbone–backbone H-bonded pairs in GB3, and the best fits correspond to  $\delta_{ZZ} = 1.40\delta_{isotropic} + 4.78$  ppm;  $\delta_{YY} = 1.68\delta_{isotropic} - 6.13$  ppm;  $\delta_{XX} = -0.08\delta_{isotropic} + 1.35$  ppm.

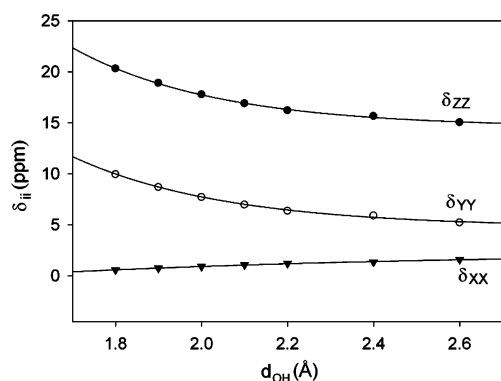


**Figure 8.** Principal components of the  $^1\text{H}^{\text{N}}$  chemical shift tensor in NMA, H-bonded to the acetamide carbonyl oxygen, obtained from DFT calculations, as a function of H-bond length,  $d_{\text{OH}}$ . The other parameters defining the relative orientation of the H-bonded pair (Figure 1) correspond to:  $\theta = 180^\circ$ ;  $\phi = 180^\circ$ ;  $\alpha = 0^\circ$ ;  $\beta = 0^\circ$ ;  $\gamma = 0^\circ$ . The three best fitted lines are  $\delta_{ZZ} = 14.6 + 1.2 \times 10^3 \exp(-3.0d_{\text{OH}})$  ppm,  $\delta_{XX} = 2.3 - 11.8 \exp(-1.1d_{\text{OH}})$  ppm, and  $\delta_{YY} = 4.8 + 0.84 \times 10^3 \exp(-2.8d_{\text{OH}})$  ppm.

by 0.9 and 0.5 ppm, respectively. However, full exploration of the impact of H-bond angles on  $^1\text{H}^{\text{N}}$  CSA would require a systematic grid search in five-dimensional space. Even for just six values of each angle,  $6^5 = 7776$  DFT calculations are required to fully sample this grid for a single  $d_{\text{OH}}$  value, which falls beyond the capabilities of our computational resources. Instead, we compare DFT results to experimental  $^1\text{H}^{\text{N}}$  chemical shifts following a procedure used by Barfield.<sup>8</sup> This procedure utilizes the model compounds NMA and acetamide to mimic the H-bond donating amide group and H-bond accepting carbonyl in GB3, and places the donating and accepting amide moieties in the relative positions of the 34 pairs of backbone amide to carbonyl hydrogen bonds, found in GB3. Considerable spread in isotropic acetamide  $^1\text{H}^{\text{N}}$  chemical shifts is calculated for the different hydrogen-bonding geometries ( $\langle\delta_{\text{iso}}\rangle = 8.7 \pm 0.9$  ppm), comparable to what is seen experimentally for the same set of amides in GB3 ( $\langle\delta_{\text{iso}}\rangle = 8.4 \pm 0.7$  ppm) (Table S5 (SI)). The DFT calculations also find a much stronger correlation between  $\delta_{ZZ}$ ,  $\delta_{YY}$  and  $\delta_{isotropic}$ , than between  $\delta_{XX}$  and  $\delta_{isotropic}$  (Figure 7B), consistent with experimental observations (Figure 7A). However, the slopes of the best fitted correlations differ somewhat between the fits of the experimental and calculated

results. For example, the best fitted slope of 1.4 for the DFT-derived correlation between  $\delta_{ZZ}$  and  $\delta_{isotropic}$  is smaller than the slope of 1.8 seen for the experimental data (Figure 7), whereas the opposite is found for  $\delta_{YY}$ , where the DFT-derived slope (1.7) is larger than the coefficient of 1.2 seen for the experimental data. Nevertheless, the computational results correlate quite well with the experimentally observed relation between CSA and isotropic chemical shift, indicating that such calculations on the NMA–acetamide pair are adequate for mimicking the effect of hydrogen bonding in a protein. We therefore proceed to investigate the impact of hydrogen bonding on  $\delta_{YY}$  and  $\delta_{ZZ}$ .

Barfield carried out DFT calculations to study the effect of hydrogen bonding on  $^1\text{H}^{\text{N}}$   $\delta_{isotropic}$ , and proposed the following empirical relation:<sup>8</sup>

$$\delta_{isotropic}(\theta_1, \alpha_3, d_{\text{OH}}) = \{c_1 \cos^2 \theta_1 + [c_2 \cos^2 \alpha_3 - c_3 \cos \alpha_3 + c_4] \sin^2 \theta_1\} \times \exp(-c_5 d_{\text{OH}}) + c_6 \quad (2)$$

where  $\theta_1$ ,  $\alpha_3$ , and  $d_{\text{OH}}$  are the structure variables (Figure 1) and  $c_i$  ( $i = 1, \dots, 6$ ) are the parameters determined from the fitting. Following the same procedure, we fitted the DFT-calculated  $\delta_{isotropic}$  values to eq 2, again yielding a good correlation ( $R_p = 0.99$ ; Figure S7 [SI]). Small differences between  $c_i$  values obtained for the fits of Figure S4 (SI) relative to Barfield's values are due to the larger basis set used in our DFT calculations.

Considering the strong correlations between  $\delta_{isotropic}$  and the principal components  $\delta_{ZZ}$  and  $\delta_{YY}$ , we use an empirical equation of the same type as eq 2 to fit  $\delta_{ZZ}$  and  $\delta_{YY}$  to H-bond geometry. The parameter  $a_5$  is fixed at 2.9, which represents the average of the values 3.0 and 2.8 obtained above when fitting the exponential dependence of the computed  $\delta_{ZZ}$  and  $\delta_{YY}$  values on  $d_{\text{OH}}$  (Figure 8). Best fits between computed CSA tensor components and H-bond geometry parameters are obtained for the following parametrizations:

$$\delta_{YY}(\theta_1, \alpha_3, d_{\text{OH}}) = \{1.25 \times 10^3 \cos^2 \theta_1 + [0.54 \times 10^3 \cos^2 \alpha_3 - 77 \cos \alpha_3 + 1.13 \times 10^3] \sin^2 \theta_1\} \times \exp(-2.9d_{\text{OH}}) + 4.6 \text{ ppm} \quad (3)$$

$$\delta_{ZZ}(\theta_1, \alpha_3, d_{OH}) = \{0.99 \times 10^3 \cos^2 \theta_1 + [1.19 \times 10^3 \cos^2 \alpha_3 + 31 \cos \alpha_3 + 0.70 \times 10^3] \sin^2 \theta_1\} \times \exp(-2.9d_{OH}) + 13.8 \text{ ppm} \quad (4)$$

With correlation coefficients  $R_p$  of 0.97 and 0.93 for  $\delta_{YY}$  and  $\delta_{ZZ}$ , respectively, values predicted by these empirical equations agree well with the DFT results (Figure S8 [SI]). Next, using the parametrizations of eqs 3 and 4 derived from the DFT results, we use these equations to predict the principal components of the CSA tensor for  $^1\text{H}^N$  atoms in GB3 that are engaged in backbone–backbone H-bonds, taking the H-bond geometries from the high-resolution X-ray structures of GB3 (PDB entry 2IGD)<sup>66</sup> and its close homologue, GB1 (entry 1PGB).<sup>67</sup> The amide protons were added to these X-ray structures using the program REDUCE.<sup>68</sup> The parameters ( $\theta_1$ ,  $\alpha_3$ ,  $d_{OH}$ ) were subsequently calculated and averaged over the two structures.

The correlations between experimental and predicted values for  $\delta_{YY}$  and  $\delta_{ZZ}$  (Figure 9) suggest that, on average, the lower  $\delta_{YY}$  and  $\delta_{ZZ}$  values observed for  $\alpha$ -helical residues as compared to  $\beta$ -strands are caused by the weaker H-bonds in the  $\alpha$ -helix, which outweighs the slight increase predicted by our above DFT results on the basis of the backbone torsion angles. DFT calculations predict an increase in  $\delta_{XX}$  with increasing  $d_{OH}$  (Figure 8), which likely contributes to the average  $\delta_{XX}$  value in  $\alpha$ -helix falling downfield from that in  $\beta$ -sheet ( $\langle \delta_{XX} \rangle_{\text{helix}} = 3.3 \pm 0.71 \text{ ppm}$ ;  $\langle \delta_{XX} \rangle_{\text{sheet}} = 2.2 \pm 0.70 \text{ ppm}$ ). The weaker H-bond interaction in  $\alpha$ -helix is corroborated by smaller average  $^3J_{NC'}$  values ( $\langle ^3J_{NC'} \rangle_{\text{helix}} = -0.37 \pm 0.22$ ;  $\langle ^3J_{NC'} \rangle_{\text{sheet}} = -0.48 \pm 0.15$  for residues for which both experimental  $^1\text{H}^N$  CSA and  $^3J_{NC'}$  are available).<sup>43</sup>

Although the correlations between H-bond parameters derived from the X-ray structures and experimental  $\delta_{YY}$  and  $\delta_{ZZ}$  values are statistically significant ( $p = 10^{-6}$ ;  $R_p = 0.75$ ; Figure 9), considerable scatter remains. It appears that much of this scatter relates to the uncertainty in the H-bond parameters. For example, when using eqs 3,4 to predict the  $\delta_{YY}$  and  $\delta_{ZZ}$  values on the basis of the coordinates of each of the individual 2IGD and 1PGB PDB entries (pairwise backbone rmsd of 0.28 Å), the scatter between the two sets of predicted  $\delta_{YY}$  and  $\delta_{ZZ}$  values ( $R_p$  of 0.79 and 0.75; Figure S9 [SI]) is nearly as high as those between predicted and experimental values.

Effects from local structural parameters, including backbone dihedral angles, side-chain type and orientation, long-range mag-

netic susceptibility, electrostatic interactions, or solvent effects, were not included in the DFT calculations used to derive eqs 3 and 4, which likely also contributes to the spread in the correlation plots of Figure 9. Furthermore, computationally more demanding methods, such as Møller–Plesset (MP) perturbation theory with complete basis set extrapolation, may improve the agreement between computed and experimentally determined chemical shift tensors.<sup>10</sup> Nevertheless, it is remarkable that even the relatively simple calculations used in the present study allow us to identify the importance of hydrogen bonding on the principal components of the  $^1\text{H}^N$  CSA tensor in a semiquantitative manner.

Unlike the impact of hydrogen bonding on the principal components of the CSA tensor, its effect on the CSA orientation ( $\beta$  angles) is less clear-cut. Experimental results suggest that, with shorter H-bond length, the angles cluster more closely to their canonical orientations (Figure S10A [SI]), a finding confirmed by our DFT calculations (Figure S10B [SI]).

A fit of the experimental data using a CSA tensor that is forced to be symmetric with respect to the peptide plane, and which therefore has only three instead of five adjustable parameters, was also carried out (Table S6 [SI]). The principal components and orientations of the resulting  $^1\text{H}^N$  CSA tensors fall close to those of the fully unrestricted fit, used above (Figure S11 [SI]). The correlations between isotropic shift and the principal components  $\delta_{ZZ}$  and  $\delta_{YY}$  obtained with this three-parameter model ( $R_p = 0.92$  for  $\delta_{ZZ}$ ;  $R_p = 0.81$  for  $\delta_{YY}$ ) are very similar to those obtained with the five-parameter fit, indicating that use of the fully unrestricted tensor analysis has not resulted in overfitting of the data. The average  $^1\text{H}^N$  CSA values obtained with the three-parameter fit are  $\sigma_{ZZ} = -6.0 \pm 1.1$ ,  $\sigma_{YY} = 0.5 \pm 0.9$ ,  $\sigma_{XX} = 5.5 \pm 1.4$ , to be compared with  $\sigma_{ZZ} = -6.2 \pm 1.0$ ,  $\sigma_{YY} = 0.5 \pm 0.9$ ,  $\sigma_{XX} = 5.7 \pm 1.3$  from the five-parameter fitting.

**Impact on TROSY  $^1\text{H}$  Line Width.** The transverse relaxation optimized spectroscopy (TROSY)  $^1\text{H}$ – $^{15}\text{N}$  HSQC experiment<sup>34</sup> relies on partial cancellation of  $^1\text{H}^N$  ( $^{15}\text{N}$ ) CSA and  $^1\text{H}$ – $^{15}\text{N}$  dipolar relaxation mechanisms to enhance spectral resolution in the  $^1\text{H}^N$  ( $^{15}\text{N}$ ) dimensions of the 2D NMR spectrum. The degree of cancellation strongly depends on the size and orientation of the CSA tensor relative to the dipolar interaction.<sup>69</sup> Our previous analysis of the impact of  $^{15}\text{N}$  CSA variations on  $^{15}\text{N}$  line width showed variations by more than 2-fold in the attainable  $^{15}\text{N}$  line width at high magnetic field strength (21 T), with optimal

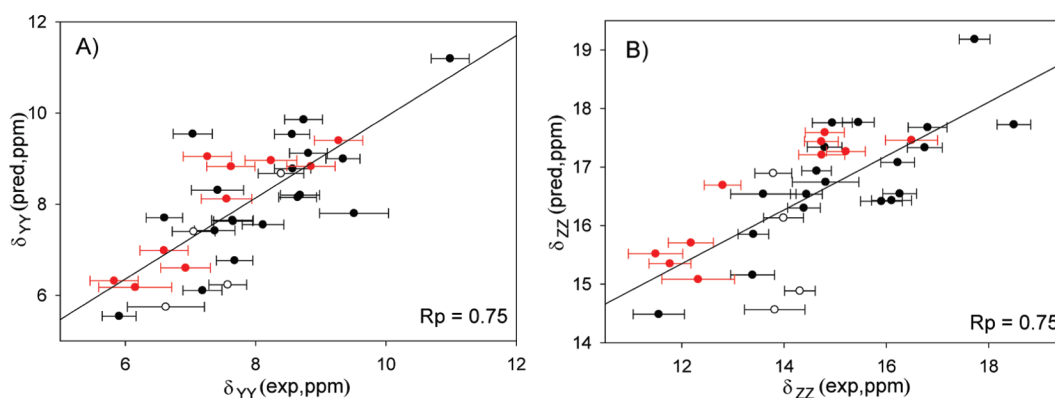


**Figure 9.** Correlations between principal components of the  $^1\text{H}^N$  CSA tensor for H-bonded amides in GB3 predicted by DFT-derived empirical equations (eqs 3,4) and experimental values for (A)  $\delta_{YY}$ , and (B)  $\delta_{ZZ}$ . For the DFT calculations, the structure parameters ( $\theta_1$ ,  $\alpha_3$ ,  $d_{OH}$ ) were averaged over those seen in PDB entries 2IGD<sup>66</sup> and 1PGB,<sup>67</sup> with the amide protons added to these as described in the text. The red filled circles correspond to residues in  $\alpha$ -helix; black filled circles are in  $\beta$ -sheet; open circles are H-bonded but neither in helix nor sheet. The best fitted lines correspond to  $\delta_{YY}(\text{pred}) = 0.89\delta_{YY}(\text{exp}) + 1.02 \text{ ppm}$ , and  $\delta_{ZZ}(\text{pred}) = 0.46\delta_{ZZ}(\text{exp}) + 9.83 \text{ ppm}$ . The RMSDs to the shown best-fitted lines are 0.55 ppm (A) and 0.71 ppm (B).

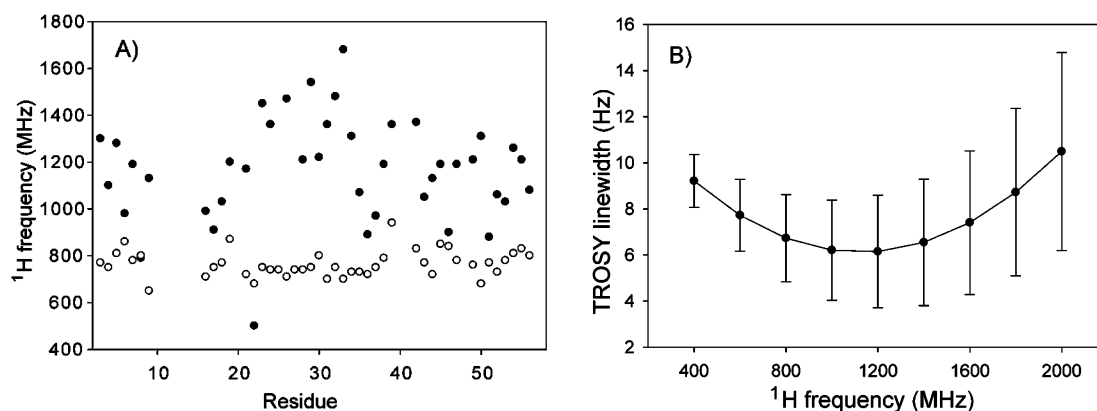


**Figure 10.** Relationship between magnetic field strength (expressed in terms of  $^1\text{H}$  resonance frequency) and TROSY effect, calculated on the basis of site specific CSA tensors determined in GB3. Results are calculated for isotropic rotational diffusion with a correlation time of 50 ns, assuming idealized two-spin approximations for each amide group (i.e., ignoring the presence of other spins and relaxation mechanisms other than  $^1\text{H}$  CSA and  $^{15}\text{N}$ – $^1\text{H}$  dipolar), using experimentally derived CSA tensors and uniform  $S^2 = 0.903$  values. (A) Magnetic field strength where the narrowest  $^1\text{H}^{\text{N}}$  (filled symbols) and  $^{15}\text{N}$  (open symbols) TROSY line widths are obtained, as a function of residue (see also Figure S12 [SI]).  $^{15}\text{N}$  TROSY line widths are calculated using the CSA tensors of ref 29. (B) Average  $^1\text{H}^{\text{N}}$  TROSY line widths and standard deviations as a function of field strength.

cancellation of the  $^{15}\text{N}$  CSA and  $^1\text{H}$ – $^{15}\text{N}$  dipolar relaxation mechanisms occurring at quite different field strengths for different residues.

Here, we evaluate the impact of variations in the  $^1\text{H}^{\text{N}}$  CSA tensor on the attainable TROSY  $^1\text{H}^{\text{N}}$  line width, again assuming an isolated  $^{15}\text{N}$ – $^1\text{H}$  spin pair approximation, i.e., neglecting dipolar interactions to remote  $^1\text{H}$ ,  $^{13}\text{C}$ , or  $^2\text{H}$  nuclei.  $^1\text{H}^{\text{N}}$  line widths for the 42 amides for which site-specific  $^1\text{H}$  CSA values were derived in GB3 are calculated for  $^1\text{H}$  frequencies of 600 and 900 MHz, assuming isotropic rotational diffusion with a correlation time  $\tau_c = 50$  ns, and a uniform generalized order parameter,  $S^2 = 0.903$  (Figure S12 [SI]). At 600 MHz,  $^1\text{H}$  line widths range from 5.2 Hz (F52) to 13.0 Hz (D22). With the exception of D22,  $^1\text{H}^{\text{N}}$  line widths at 900 MHz are narrower than at 600 MHz. Evaluating the calculated  $^1\text{H}^{\text{N}}$  line widths as a function of magnetic field strength, using our experimentally derived  $^1\text{H}^{\text{N}}$  CSA tensors, indicates that the field strength where the  $^1\text{H}^{\text{N}}$  line width is narrowest varies strongly from residue to residue, far more than for  $^{15}\text{N}$  (Figure 10A). On average, the narrowest line widths are obtained at a  $^1\text{H}$  frequency of 1.2 GHz (Figure 10B), requiring a magnetic field strength of 28 T, not yet commercially available. As expected, the spread in predicted  $^1\text{H}^{\text{N}}$  line widths increases at higher magnetic fields, due to the quadratic increase in the importance of  $^1\text{H}$  CSA as a relaxation mechanism. Complete cancellation of the dipolar and CSA mechanisms can only occur if the  $^1\text{H}^{\text{N}}$  CSA tensor is axially symmetric, with its unique axis parallel to the N–H bond vector, a condition that does not apply for any of the amide protons in GB3. The deviations from this condition determine what optimal line width is achievable for any given proton, and at what field the cancellation of the two relaxation mechanisms reaches that maximum.

Clearly,  $^1\text{H}$  chemical shift anisotropy is an exquisitely sensitive reporter on local structure. However, experimental studies of  $^1\text{H}$  CSA in biological macromolecules have been rather sparse. In part, this may be due to difficulties in studying individual  $^1\text{H}$  CSA tensors by solid state NMR spectroscopy.

Nevertheless, with increases in magnetic field strengths, and novel experimental cross-correlated relaxation methods as well as reliable RCSA measurement procedures based on magic angle spinning of liquid crystals, obtaining accurate  $^1\text{H}$  CSA parameters appears well within reach. Analysis of the  $^1\text{H}^{\text{N}}$  CSA tensors in our study did not require the assumption of symmetry with respect to the peptide plane for the  $^1\text{H}^{\text{N}}$  CSA tensor but found that the experimentally derived tensors are close to being symmetric. Future analyses, therefore, will require less experimental information to derive the three parameters needed for defining such symmetric tensors, rather than the five parameters evaluated in the current study.

**Acknowledgment.** We thank Dennis A. Torchia and Jinfa Ying for helpful discussions, and Werner Maas and Jochem Struppe (Bruker Instruments) for help with the MAS measurements. This work was supported in part by the Intramural Research Program of the NIDDK, NIH, by the Intramural AIDS-Targeted Antiviral Program of the Office of the Director, NIH, and by NIH Grants P41RR02301 (BRTP/NCRR) and P41GM66326 (NIGMS) to G.C.

**Supporting Information Available:** Complete ref 47; three figures with pulse diagrams used for the measurement of cross-correlated relaxation; one figure showing RDC SECONDA analysis results; one figure comparing  $\Gamma^{\text{CSA,NH}}$  values on different mutants; one figure comparing  $\beta_1$  and  $\beta_2$  angles of the  $^1\text{H}^{\text{N}}$  CSA tensors; one figure comparing DFT-derived isotropic  $^1\text{H}^{\text{N}}$  shifts for H-bonded NMA–acetamide pairs with results from a best-fitted empirical equation; one figure comparing DFT-derived principal components of the  $^1\text{H}^{\text{N}}$  CSA tensor for two different X-ray structures; one figure correlating orientation of the CSA tensor to H-bond length; one figure comparing best-fitted CSA principal components derived using the three- and five-parameter CSA models; one figure showing calculated  $^1\text{H}$  TROSY line widths; two tables with experimental  $^1\text{H}^{\text{N}}$  and  $^{13}\text{C}$  RCSA values; one table with experimental cross-correlation rates; two tables with CSA tensors using either three or five parameters; one table with DFT-derived CSA principal components for H-bond geometries found in GB3. This material is available free of charge via the Internet at <http://pubs.acs.org>.

JA103629E

- (66) Derrick, J. P.; Wigley, D. B. *J. Mol. Biol.* **1994**, *243*, 906–918.  
 (67) Gallagher, T.; Alexander, P.; Bryan, P.; Gilliland, G. L. *Biochemistry* **1994**, *33*, 4721–4729.  
 (68) Word, J. M.; Lovell, S. C.; Richardson, J. S.; Richardson, D. C. *J. Mol. Biol.* **1999**, *285*, 1735–1747.  
 (69) Fushman, D.; Cowburn, D. *Methods Enzymol.* **2001**, *339*, 109–126.